Int. J. Nano Dimens., 11 (4): 377-391, Autumn 2020

ORIGINAL ARTICLE

Photocatalytic degradation of water pollutant dye by solid state synthesized $Ni_{1-x}Ln_xSb_2O_6$ (Ln=Eu, Gd, Ho and Yb) nanocomposites

Neda Papi[1], Alireza Hakimyfard[1], Nemat Tahmasebi[1], Mohammad Samimifar[2]*

[1]*Department of Physics, Faculty of Science, Jundi-Shapur University of Technology, Dezful, Iran*
[2] *Department of Chemistry, Faculty of Science, Jundi-Shapur University of Technology, Dezful, Iran*

Received 06 February 2020; revised 18 July 2020; accepted 22 July 2020; available online 02 August 2020

Abstract

Nanostructured $Ni_{1-x}Ln_xSb_2O_6$ (Ln = Eu, Gd, Ho and Yb) powders were synthesized via stoichiometric 1:2 Ni:Sb molar ratio by solid state reaction at 800 °C for 8 h using $Ni(NO_3)_2$, Sb_2O_3, Eu_2O_3, Gd_2O_3 and Ho_2O_3 raw materials. The synthesized materials were characterized by X-ray diffraction (XRD) technique. Structural analyses were done by *FullProf* program employing profile matching with constant scale factor. The results showed that the patterns had a main orthorhombic $NiSb_2O_6$ crystal structure with P42/mbc space group. The morphologies of the synthesized materials were studied by field emission scanning electron microscope (FESEM) which showed that the synthesized samples had sponge morphology. Ultraviolet – Visible (UV-Vis) spectroscopy showed that the smallest direct optical band gap energies were in the ranges of 1.6 to 1.8 eV suggesting a high efficient photocatalytic activity. Photocatalytic performance of the synthesized nanomaterials was investigated for the degradation of pollutant Malachite Green (MG) in aqueous solution under visible light condition. It was found that the optimum conditions were 0.04 mL H_2O_2, 30 mg catalyst, and 35 min reaction time. It was found that the synthesized $NiSb_2O_6$ nanocatalyst had very good efficiency in aqueous solution under the optimized conditions at the presence of visible light irradiation. The degradation yield at the optimized conditions was 96 %. The optimum photocatalytic condition was used to study the performance of the other synthesized materials in the photocatalytic degradation process.

Keywords: *Dye Degradation; Full Prof; Malachite Green; Nanocatalyst; Solid State.*

How to cite this article

Papi N., Hakimyfard AR., Tahmasebi N., Samimifar M. Photocatalytic degradation of water pollutant dye by solid state synthesized $Ni_{1-x}Ln_xSb_2O_6$ (Ln=Eu, Gd, Ho and Yb) nanocomposites. Int. J. Nano Dimens., 2020; 11 (4): 377-391.

INTRODUCTION

Transition metal antimonates with the general formula MSb_2O_6 (M = Zn, Cd, Pb, Ni, etc.) have been investigated primarily because of their interesting structure, electronic, and optical properties. These oxides crystallize in the orthorhombic crystal structure in the space group P42/mnm. $NiSb_2O_6$ has attracted attention due to its magnetic photocatalytic, as transparent conductor, and sensors properties [1]. It finds applications as antimony metal oxide catalyst and in resistors [2-4]. Several methods have been reported for the synthesis of $NiSb_2O_6$ materials including solid state method using $NiSO_4$ and $NaSbO_3$ at 500 °C

* Corresponding Author Email: *: ahakimyfard@jsu.ac.ir*
ahakimyfard@yahoo.com

[1], solid state method using NiO and Sb_2O_4 at 900 °C [2], sol-gel [4,5], hydrothermal [6], solid state method using Sb_2O_3 and NiO at 800 °C for 72 h [7], solid state method using NiO and Sb_2O_3 at 1450 °C for 48h [8], microwave - assisted colloidal [9] and recently a solid state [10] methods.

MG is classified in the dyestuff industry as a triarylamine dye and used in pigment industry. MG has been used extensively in the leather, paper, silk, cotton, and jute dyeing processes. It is also used as an antifungal and anti-protozoan agent in fisheries and aquaculture industry [11, 12]. MG is a non-biodegradable dye pollutant and has now become a highly controversial compound due to the risks it poses to the consumers of treated fish, including its effects on the immune and reproduction systems. Furthermore, MG and its metabolites are known to cause mutagenic, carcinogenic, and teratogenic effects to living organisms [13]. It should not be used for beverages, food, medicines because it causes skin irritation, blurred vision or cause interference. Its inhalation may cause irritation to the respiratory tract, and in large quantities can cause tissue damage and inflammation of kidneys [14]. Pure and functionalized metal oxides nanopowders have found several catalytic and photocatalytic applications [15,16]. Recently, several metal oxides have been used for the degradation of MG under different conditions including: MoS_2/TiO_2 nanocomposite [17], $PbCrO_4$ [18], TiO_2/ZrO_2 [19], Ni_x : TiO_2 [20], TiO_2 [21], V doped ZnO [22], TiO_2 [23], $Ni_{1-x}Co_xFe_2O_4$ [24], $Pt/TiO_2/SiO_2$ [25], $Sr_2As_2O_7$ [26], etc.

To find optimum values of parameters affect on the malachite green photodegradation conditions, experimental design method is used. In the method, a Design Of Expert (DOE) using Central Composite Design (CCD) is applied.

Design of Expert is a piece of software designed to help with the design and interpretation of multi-factor experiments. In photocatalytic processes, the software is used to help researchers design an experiment to see how much a photocatalyst and H_2O_2 are used and how many minutes are needed to finalize the degradation process. The software offers a wide range of designs, including factorials, fractional factorials and composite designs. Design Expert offers computer generated D-optimal designs for cases where standard designs are not applicable, or where we wish to augment an existing design [27, 28]. A Box-Wilson Central Composite Design, commonly called a central composite design (CCD), contains an imbedded factorial or fractional factorial design with centre points that is augmented with a group of points that allow estimation of curvature. If the distance from the centre of the design space to a factorial point is ±1 unit for each factor, the distance from the centre of the design space to appoint is $|\alpha| > 1$. The precise value of α depends on certain properties desired for the design and on the number of factors involved [27, 28].

In the present study, a facile one-step solid state method was explored for the synthesis of nanostructured Ln-doped $NiSb_2O_6$ powders using $Ni(NO_3)_2$, Sb_2O_3 and Ln_2O_3 raw materials at 800 °C for 8 h. To the best of our knowledge, there is no information available in the literature about doping the Ln_2O_3 into $NiSb_2O_6$ crystal system under the present conditions. The direct optical band gap energies of the as-prepared $NiSb_2O_6$ nanomaterials were initially estimated from ultraviolet-visible spectra. Photocatalytic performance of the synthesized $NiSb_2O_6$ nanomaterials is investigated for the degradation of MG under solar light condition. Experimental design method was used to optimize factors affecting the degradation reaction. The factors are the amount of the nanocatalyst, H_2O_2 and the reaction time.

EXPERIMENTAL

General remarks

All chemicals were of analytical grade, obtained from commercial sources, and used without further purification. Phase identifications were performed on a X-ray powder diffractometer D5000 (Siemens AG, Munich, Germany) using CuK_α radiation. The morphologies of the obtained materials were studied by a field emission scanning electron microscope (Hitachi FE-SEM model S-4160). Absorption spectra were recorded on an Analytik Jena Specord 40 (Analytik Jena AG Analytical Instrumentation, Jena, Germany). The Software used for the design of experiment (DOE) was Design Expert 7. Measurement of the photocatalytic activity of the synthesized samples was investigated in the presence of H_2O_2 (30%, w/w) under visible light source. A Shimadsu, UV-Vis 1650 PC spectrophotometer was used to measure the absorbance spectra of MG in the range of 200–700 nm by a quartz cell with an optical path of 1 cm. A BEL PHS-3BW pH-meter with a combined

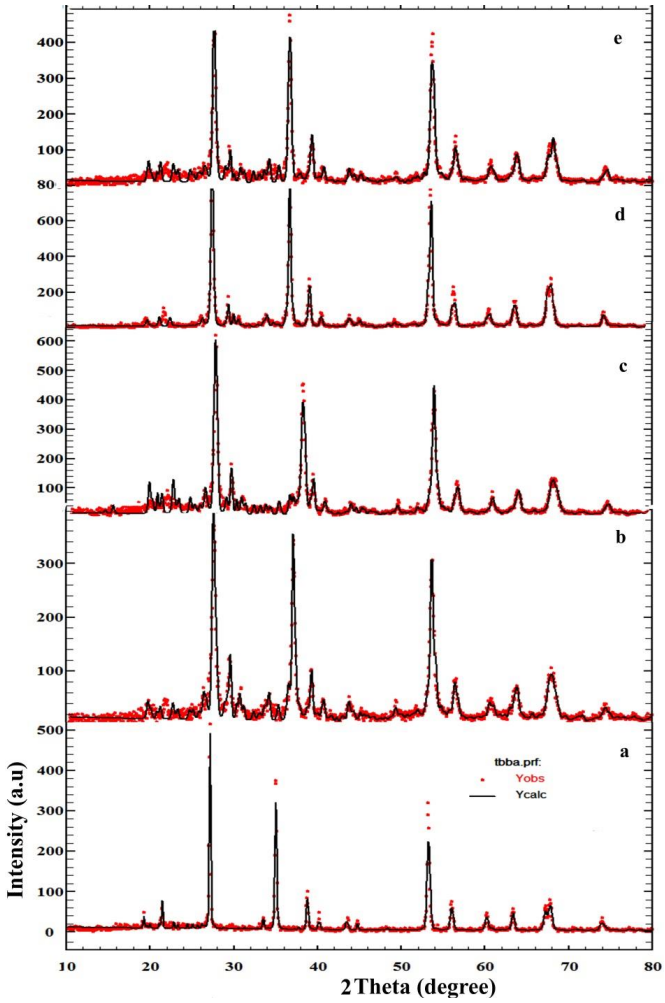

Fig. 1. XRD patterns of a) pure $NiSb_2O_6$, b) S_1, c) S_2, d) S_3 and e) S_4 refined by rietveld analysis.

glass-Ag/AgCl electrode was used for adjustment of test solution pH.

Catalyst preparation

In a typical solid state synthetic experiment, 0.01 mmol of Ln_2O_3 (Eu_2O_3 (S_1), Gd_2O_3 (S_2), Ho_2O_3 (S_3) and Yb_2O_3 (S_4)), 1 mmol of Sb_2O_3 (Mw = 291.5 $gmol^{-1}$) and 1 mmol of $Ni(NO_3)_2.6H_2O$ (MW = 290.7 $gmol^{-1}$) were mixed in a mortar and ground until a nearly homogeneous powder was obtained. The obtained powder was added into a 25 mL crucible and treated thermally in one step at 800 ºC for 8 h. The crucible was then cooled normally in the furnace to the room temperature.

RESULTS AND DISCUSSIONS

Characterization

The XRD patterns of the as-synthesized Ln-doped $NiSb_2O_6$ samples are reported in Fig. 1 (a-e) with the results of the profile matching analyses (full lines). Fig. 1 shows the XRD analyses of the obtained samples in the θ-2θ geometry with Cu-Kα radiation. The structural results done by *FullProf* program showed that the patterns had a main $NiSb_2O_6$ tetragonal crystal structure with space group of $P4_2/mnm$ [7-9, 29, 30]. S_0 is the as reported data corresponded to the pure $NiSb_2O_6$ [10]. According to the rietveld analyses shown in Fig. 1 (b-e), it is clear that doping the lanthanide ions reduced the purity of $NiSb_2O_6$. The impurity phases are Sb_2O_5 [31], Sb_2O_3 [32] and NiO [33]. The data reveal that when the dopant ions are introduced into the crystal system, the volume of the as-synthesized samples are decreased slightly. However we know that the ionic radii of the lanthanide ions are larger than those of Ni and Sb ions, the surprising observation can be due to the lanthanide 4f contraction effect on the cell volume

Table 1. Cell parameter, crystallite size, dislocation density, strain, and interplanar spacing of the as-synthesized nanomaterials.

Sample	a(Å)	c(Å^3)	V(Å^3)	2θ	Sinθ	cosθ	B	D (nm)	δ (lines/m^2)	ε	d_{Calc} (Å)
S_0	4.631	9.193	197	27.207	0.2352	0.9719	0.00423	34	8.65	1.03	2.020
S_1	4.619	9.141	195	27.721	0.2396	0.9710	0.00466	31	10.4	1.13	2.015
S_2	4.593	9.135	193	27.814	0.2403	0.9707	0.00466	31	10.4	1.13	2.004
S_3	4.591	9.098	192	27.905	0.2411	0.9705	0.00466	31	10.4	1.13	2.003
S_4	4.561	9.010	187	27.566	0.2382	0.9712	0.00466	31	10.4	1.13	1.989

of the final doped products.

Some crystallographic parameters were calculated and summarized in Table 1 to study the dopant effects on the crystallographic property of the as-synthesized nanomaterials.

The lattice volume is obtained by the below formula (Table 1):

$$V = a.b.c \quad (1)$$

The data indicates that the intercalation of the dopant ions into $NiSb_2O_6$ crystal system has occurred into the larger crystal cavity.

The interplanar spacing (d) value is also calculated by the below formula:

$$\frac{1}{d^2} = \left(\frac{h^2}{a^2} + \frac{k^2}{b^2} + \frac{l^2}{c^2} \right) \quad (2)$$

By using the peak with the highest intensity at 2θ ≈ 27.56 º and the (h k l) value of (2 1 1), the above equation is changed to the following formula:

$$\frac{1}{d^2} = \left(\frac{4}{a^2} + \frac{1}{b^2} + \frac{1}{c^2} \right) \quad (3)$$

The grain size data (D) of the obtained nanomaterials is calculated by Scherrer equation (Table 1):

$$D = \frac{K\lambda}{B_{\frac{1}{2}} cos\theta} \quad (4)$$

Where D is the entire thickness of the crystalline sample, λ is the X-ray diffraction wavelength (0.154 nm), K is the Scherrer constant (0.9), $B_{1/2}$ of FWHM is the full width at half of its maximum intensity and θ is the half diffraction angle where the peak is located. As could be found from the data, the grain size of the as-synthesized doped materials has been decreased when the dopant ions are introduced into the crystal system.

Also, the dislocation density (δ) [(lines/m^2)10^{14}] value related to the number of defects in the crystal is calculated by the following relationship:

$$\delta = \frac{1}{D^2} \quad (5)$$

As it is indicated in Table 1, it is found that the δ value is increased when the dopant ions are introduced into the crystal system. However, the data show that doping the lanthanide ions into the crystal cavity increases the dislocation density considerably that can be due to the decreasing the nanomaterials grain sizes.

The strain ε (10^{-3}) values are also calculated by the following formula:

$$\varepsilon = \frac{\beta_{hkl} cos\theta}{4} \quad (6)$$

Table 1 includes the variation of ε as a function of the dopant ion type in the crystal system. The data show that the value of strain for $NiSb_2O_6$ is small. But, when the lanthanide ions are doped into the crystal system, the strain value is increased. This observation is probably due to the retrograding the crystallinity degree of the obtained material.

Morphology analysis

Fig. 2 (a-d) related to S_1 – S_4, respectively, present the FESEM images of the as-prepared $NiSb_2O_6$ nanomaterials. As previously reported, pure $NiSb_2O_6$ has particle morphology with the average size of 40 – 50 nm. However, when the dopant ions were introduced, the morphology was changed to homogeneous sponge structure. The data reveal that doping the lanthanide ions improved the morphology and reduced the particle size of the final product. The data reveals that the crystallite sizes are 30 – 40, 20 – 30, 20 – 30 and 20 – 30 nm for S_1, S_2, S_3 and S_4, respectively.

Energy dispersive X-ray analysis

Fig. 3 (a – d) illustrates the EDX analysis spectra of S_1-S_4, respectively, with 0.01 mmol of the dopants ions into the crystal system studying the compositional analysis of Eu^{3+} or Gd^{3+} or Ho^{3+} and/

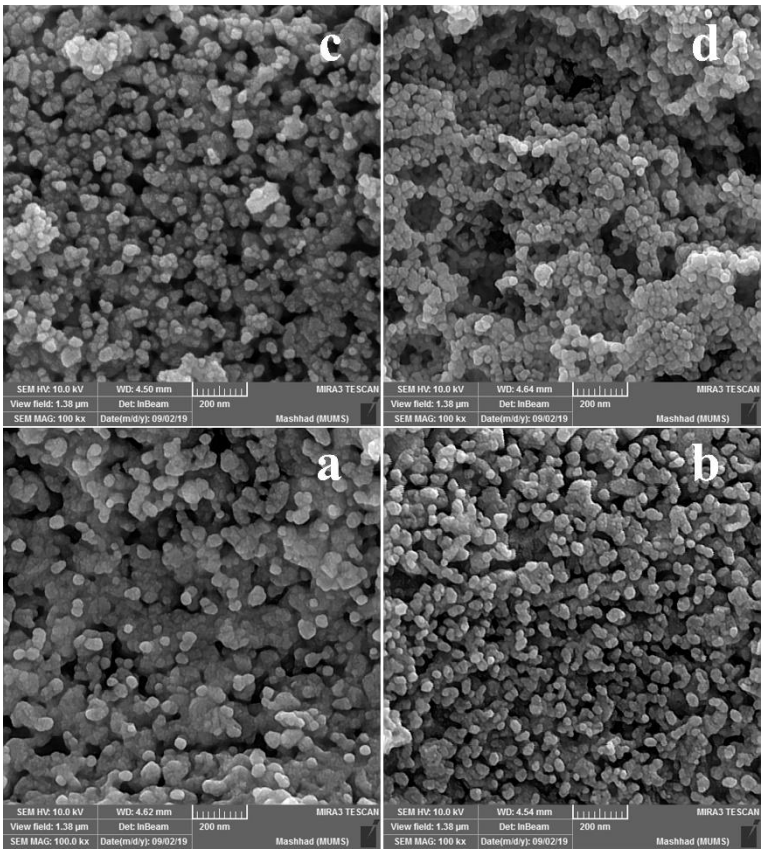

Fig. 2. FESEM images of a) S_1, b) S_2, c) S_3 and d) S_4.

or Yb^{3+} in $NiSb_2O_6$. The peaks corresponded to Eu or Gd or Ho or Yb and (Ni, Sb and O) atoms present in the samples are labeled. The respective energy positions and the specific X-ray lines from various elements are also indicated. Besides, the A% values of the dopants in the obtained samples and studying the capacity of $NiSb_2O_6$ to accept the ions in the crystal systems is reported. The A% values are 0.48, 0.64, 0.43 and 0.57 for Eu^{3+}, Gd^{3+}, Ho^{3+} and Yb^{3+} doped nanomaterials. The data reveal that when a heavier lanthanide ion is included in the crystal system, the capacity of the crystal system to accept the ions is decreased.

Optical Properties

The UV-Vis spectra and direct optical band gap energies of the as-synthesized $NiSb_2O_6$ nanocomposites which obtained from UV-Vis absorption spectra are shown in Fig. 4. According to the results of Pascual et al., the relation between the absorption coefficient and incident photon energy can be written as $(\alpha hv)^n = A(hv - E_g)$, where A is a constant and E_g is the direct band gap energy if n=2. The Band gap energy was evaluated from extrapolating the linear part of the curve to the energy axis. The smallest value of the direct optical band gap energies are 1.6 and 1.8 eV for S_1, S_2, S_3 and S_4, respectively.

Photocatalytic activity

The photocatalytic activity of the previously synthesized $NiSb_2O_6$ sample (S_0) was investigated for the degradation of MG in the presence of H_2O_2 (30%, w/w) under visible light irradiation. The other synthesized nanomaterials were also studied for their photocatalytic performance at the optimized conditions obtained by $NiSb_2O_6$ nano-photocatalyst. To prepare 45 ppm MG dye solution, 11.2 mg of MG powder was dissolved in 250 mL of deionized water. The pH value of the obtained solution was 4. In a typical photocatalytic experiment, certain amount (g) of the as-synthesized $NiSb_2O_6$ photocatalyt was added to 70 mL of the prepared MG aqueous

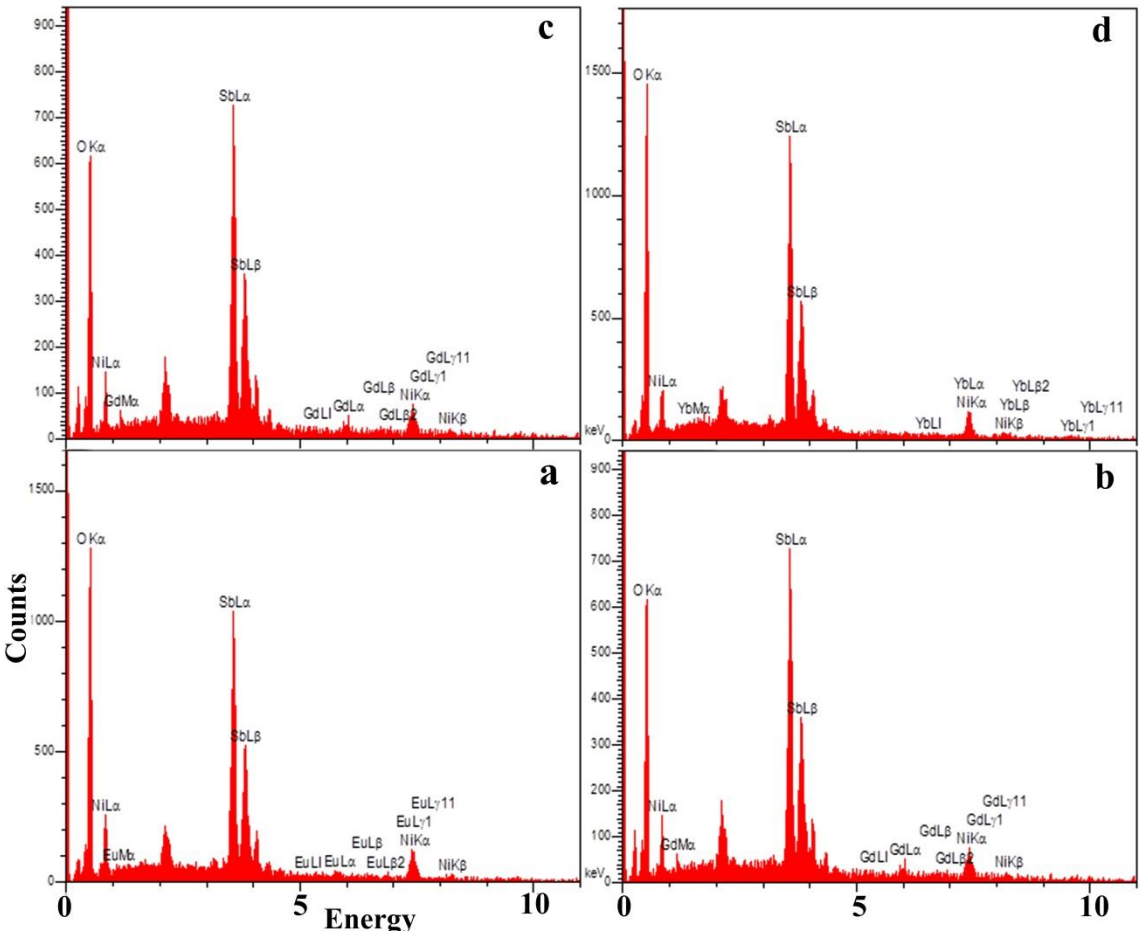

Fig. 3. Energy dispersive X-ray analysis of a) S_1, b) S_2, c) S_3 and d) S_4.

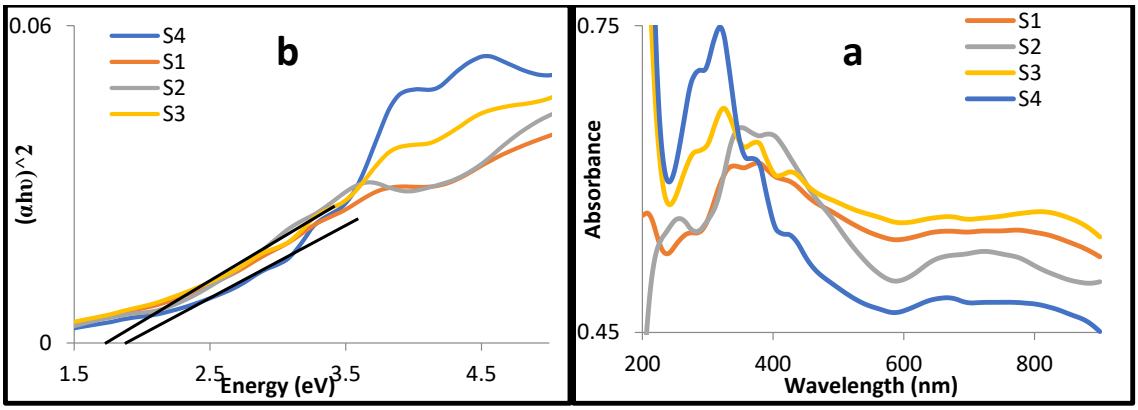

Fig. 4. Plots of a) UV-Vis absorption spectrum and b) direct optical band gap energies of the as-synthesized nanocomposites.

solution and sonicated for 10 min in a dark room to establish an adsorption/desorption equilibrium between MG molecules and the surface of the photocatalyst. Afterwards, certain volume (mL) of H_2O_2 was added into the mixture solution, followed by further magnetic stirring under solar

light condition. When the designed time (min) was elapsed, the solution was drawn out and the photocatalyst was separated by centrifugation in order to measure the absorption spectra of MG and calculate the MG concentration using UV-Vis spectrophotometry. The mixture was kept at a constant stirring of 300 rpm at the temperature of the experiment. The photodegradation yield (%) of MG was calculated by the following formula:

$$\left(\frac{A_0\text{-}A_t}{A_0}\right)\times 100 \quad (7)$$

where, A_0 and A_t represent the initial absorbance of MG at 610 nm and the absorbance at time t, respectively.

Experimental design for achieving optimal conditions in MG degradation process

Researchers utilize two different approaches to obtain the optimal conditions in chemical reactions, namely one-at-a-time and experimental design methods. Recently, the experimental design method is receiving more attention. In the method, different experiment factors affect each other. This is not considered in the one-at-a time approach. Full factorial design is one of the basic designs. In this design, all possible combinations of the factors and their settings are simultaneously considered. Assume that there is k investigating variables and each variable could be set to m distinctive levels. The number of possible combinations of the factors and their settings will then be m^k. In chemical systems, three levels of the factor setting is common because such designs allow the determination of all main effects and all interaction effects with small number of experiment .

Full factorial design is one of the most powerful design tools in which three levels of each factor are used to design a set of proposed runs. In this design, the experimental points are embedded at the center (central points) and on the midpoints of the edges. In full factorial method, the relation between the factors and response is theoretically modeled which causes the reproducibility of the results. So, it is possible for experiments to elucidate the results. Response surface methodology (RSM) is a mathematical and statistical method analyzing experimental design by applying an empirical model.

Design of experiments (DOE) is a targeted and planned method for finding the relationships between independent variables, their overall impact on dependent variables and obtaining maximum information from the minimum possible experiments. The Response surface methodology (RSM) using input data, offers the graphical relationship between responses and variables, and performs multiple regression analysis [27,28].

The adequacy of the applied model is checked using analysis of variance (ANOVA) which needs some replicate experiments.

In the present MG pollutant dye degradation process, the goal was to determine how much nanocatalyst should be used, and at which time and H_2O_2 volume the degradation should be monitored. The response was the yield of degradation (Y%). Different possible combinations of these factors were designed which are reported in Table 2. All the experiments were done at two days with random order. The central composite design (CCD) was chosen to model and optimize the proposed procedure based on S_0. A three-level CCD with three factors (H_2O_2 (A), catalyst (B) and time (C)) was used to investigate the effects of factors. The condition of 20 experiments designed by CCD accompanied to dye degradation percentage (response (R%)) are also given in Table 2. The experimental range and levels of independent variables are shown in Table 3. As shown in Table 3, the independent variables (H_2O_2 volume (A_1), catalyst amount (A_2) and stirring time (A_3)) are given in the coded form (-α, -1, 0, +1, +α).

The statistical test of ANOVA analyzes the variances and examines the significance of the factors and their interactions on themselves and other factors. Then, with the help of the RSM, the validated model is plotted in three dimensions and interpreted to find the best conditions for the process. ANOVA of regression parameters for the quadratic model was computed in Table 4. The Fisher's F test in the ANOVA analysis was performed to compare either model variance or factors with residual (error) variance, where the larger F-values and the smaller P-values indicate the more significant terms of the model [27, 28]. This ratio is called an F-distribution (F-value), varying from 1 to larger values. Values far from 1, exceeding from the tabulated F-value, provide evidence against the null hypothesis, indicating the significance of the regression parts of the fitted models. Equivalently, the null hypothesis is rejected when p-value is less than a significant

Table 2. Experimental and predicted results of applied model for photo-catalytic malachite green degradation over $NiSb_2O_6$.

Run	H_2O_2 (mL)	Catalyst (g)	Time (min)	Y(%)
1	0.06	0.04	50	100
2	0.02	0.04	50	97
3	0.02	0.04	20	85
4	0.04	0.03	35	93
5	0.04	0.03	35	91
6	0.06	0.02	50	98
7	0.04	0.03	35	93
8	0.06	0.02	20	74
9	0.04	0.03	35	93
10	0.02	0.02	20	74
11	0.02	0.02	50	97
12	0.06	0.04	20	92
13	0.07	0.03	35	89
14	0.04	0.03	10	67
15	0.01	0.03	35	80
16	0.04	0.03	60	95
17	0.04	0.03	35	90
18	0.04	0.01	35	78
19	0.04	0.03	35	90
20	0.04	0.05	35	94

Table 3. Ranges of operational parameters for experimental design in CCD.

Factor Name	Units	Low Actual	High Actual	Low Coded	High Coded
A	H_2O_2 (mL)	0.02	0.06	-1	1
B	Catalyst (mg)	20	40	-1	1
C	Time (min)	20	50	-1	1

Table 4. ANOVA test results for degradation of malachite green by photo-catalytic process.

Source	Sum of Squares	df	Mean Square	F Value	p-value Prob > F	
Block	130.21	1	130.21			
Model	1443.41	8	180.43	65.88	< 0.0001	significant
A-H_2O_2	50.02	1	50.02	18.26	0.0016	
B-Catalyst	245.55	1	245.55	89.66	< 0.0001	
C-Time	953.12	1	953.12	348.03	< 0.0001	
AB	10.13	1	10.13	3.7	0.0834	
BC	91.12	1	91.12	33.27	0.0002	
A^2	18.39	1	18.39	6.71	0.0269	
B^2	5.18	1	5.18	1.89	0.1992	
C^2	80.7	1	80.7	29.47	0.0003	
Residual	27.39	10	2.74			
Lack of Fit	24.39	6	4.06	5.42	0.0619	not significant
Pure Error	3	4	0.75			
Cor Total	1601	19				

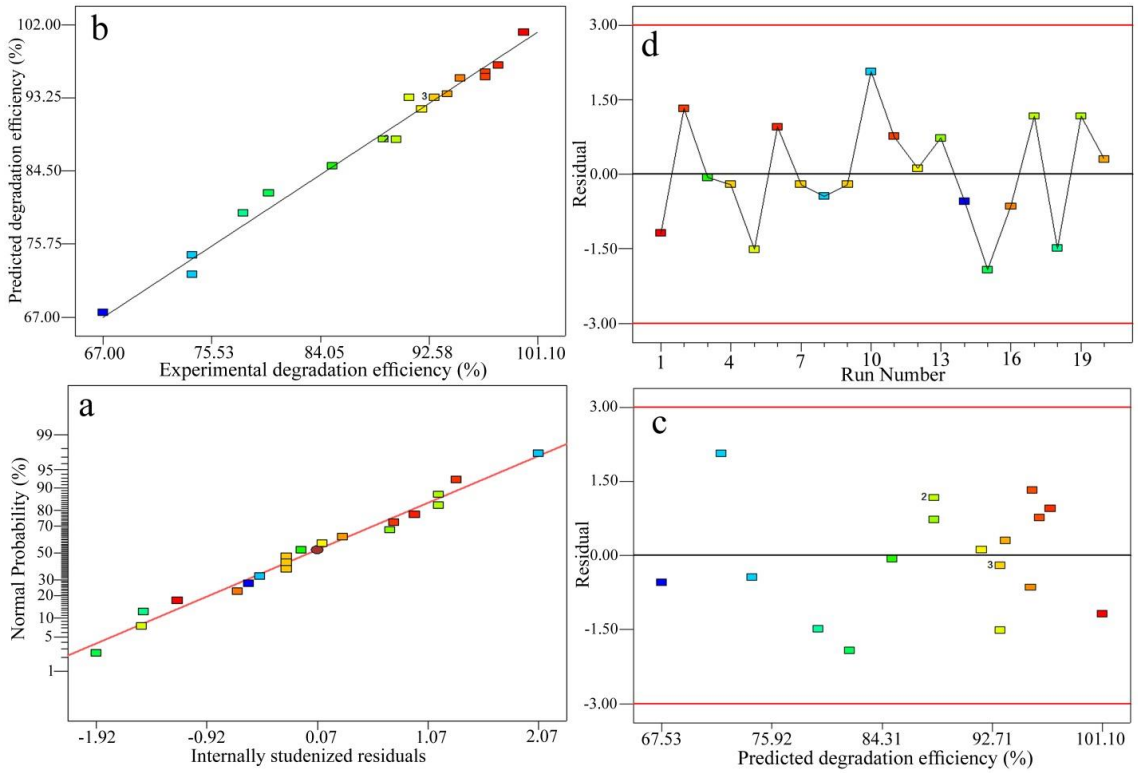

Fig. 5. a) the normalized possibility versus studentized residual, b) the residual versus degradation efficiency, c) predicted versus the experimental degradation efficiency and d) residuals versus run number data.

level. In order to obtain the significant and reliable model at 95% confidence level, the p-values for the fitted model and its corresponding terms should be smaller than 0.05. The p-value of the present regression was smaller than 0.05, showing that the model was significant at a high confidence level (95%). A further assessment of the fitted model can be carried out using the lack-of-fit test. Via this statistical test, the residual part is sub-divided into pure error and lack-of-fit. In other words, it distinguishes the random error from the systematic one, causing the lack of fitting of the model with specific order. Therefore, at the 95% confidence level, the p-values for the lack-of-fit should be greater than 0.05, which is not significant. As shown in Table 4, the outcomes of ANOVA are completely in agreement with the above statements.

Also the coefficient of determination (the R-square, adjusted–R-square) was used to express the quality of fit of polynomial model equation. In this case, R^2 of variation fitting for Y% = 97 indicated a high degree of correlation between the response and the independent factors (R^2 = 0.9821). Also, the high value of adjusted regression coefficient (R^2-adj = 0.9643) indicated high significance of the proposed model. This means that, the difference between experimental and the predicted responses is negligible. Also the predicted R-squared value (0.8803) was reasonable. It indicates the high accuracy and reliability of the developed mode to determine the response value shown in Fig. 5.

Fig. 5 represents a plot of the predicted versus the experimental degradation efficiency. This figure shows a good agreement between the predicted and experimental degradation efficiency (R^2 = 0.9821) and represents the adequacy and significance of the model. Also, Fig. 5 indicates the normal plots of the predicted versus the observed response for the degradation efficiency. As it is evident in this figure, the data points obtained consistently appear on a straight trend line, demonstrating that there is no obvious dispersal. Dispersal of residuals is also shown in Fig. 5 (a-d).

The observed data of the factorial design was fitted to a quadratic response model. Prior to the analysis, low and high factor levels were coded

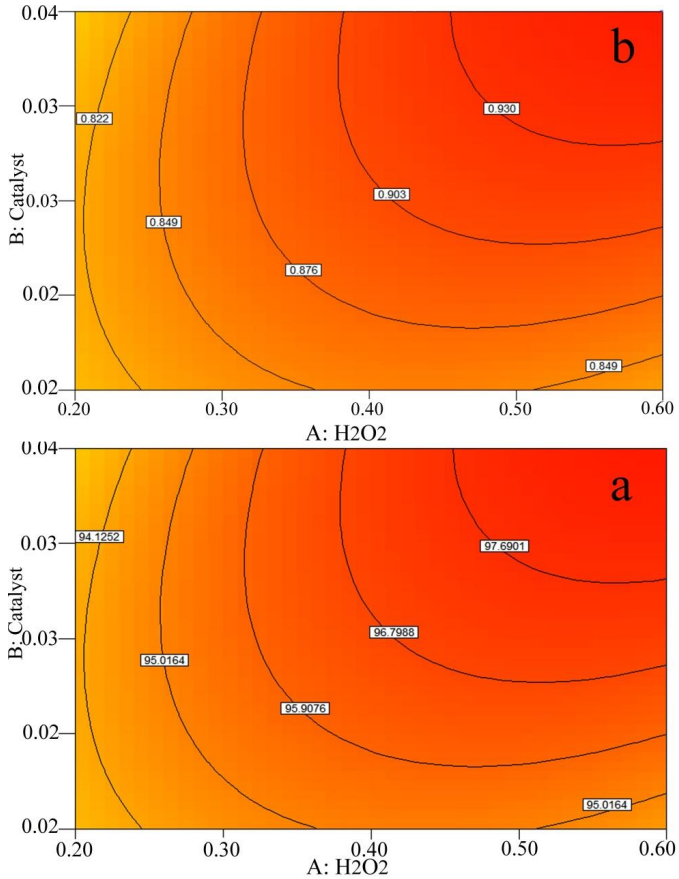

Fig. 6. Plots of a) degradation yield and b) desirability factor at 50 min.

to -1 and +1, respectively. Equation 1 shows the relation between the factors and the yield of the reaction, Y%, based on the first order model:

$Y\%=15.07191+15.29258\times A+1346.28964\times B+1.96845\times C+562.5\times A\times B-22.5\times B\times C-28.24838\times A^2-5996.05179\times B^2-0.010522\times C^2$ (Equation 1)

Fig. 6 shows the two dimensional plots of degradation yield associated with the desirability plots for catalyst amount versus H_2O_2 volume factors at the constant 50 min photocatalytic reaction time. The data show that the degradation yield and desirability is high when the catalyst amount and H_2O_2 volume are 30 mg and 0.04 mL, respectively. In this case, the desirability is 0.93 and degradation yield is 97 %.

To illustrate the effect in the above model, the three–dimensional response surface plots of the response are shown in Fig. 7. To show the effects of the three factors on the photodegradation process, the response surface methodology (RSM) was used. Fig. 7 (a-c) represents the 3D plots related to the interaction of AC, AB and BC, respectively. The semi-curvatures of these plots indicate the interaction between the variables. In other words, at a certain reaction time, when H_2O_2 and catalyst amounts increase, dye removal percentage improves. This means that, the mass transfer of dye molecule enhances on the surface of the catalyst and the dye adsorption process on the catalyst reaches equilibrium state quickly. Also, by increasing the catalyst amount, further surface area of adsorbent is available for dyes molecules leads to enhance the dyes removal percentage.

Fig. 8 (a and b) illustrate the photocatalytic performance of the as-synthesized nanomaterials. Fig. 8a, presents MG degradation spectra by S_0. The data confirms the high performance of the sample to degrade MG by the mentioned photocatalytic conditions. Fig. 8 b shows a comparison study of the catalytic performance among the as-synthesized nanomaterials. As could be seen from the data, a non-considerable decrease in the catalytic activity is found when the dopant ions are introduced into the crystal system.

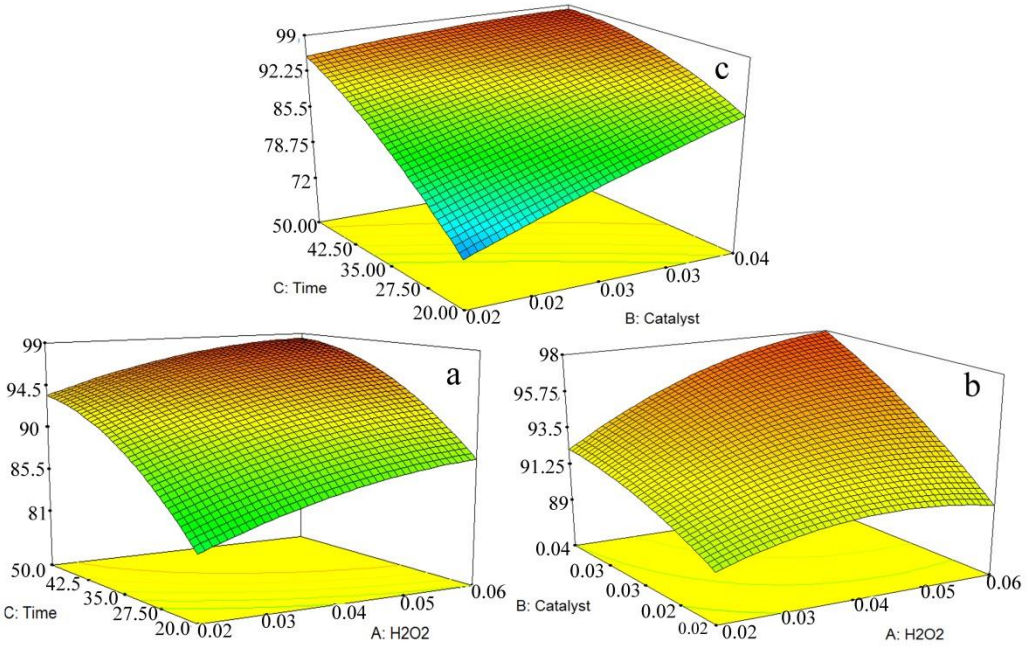

Fig. 7. 3D surface plots of a) AC, b) AB and c) BC interaction of the factors affect on the removal of MG dye.

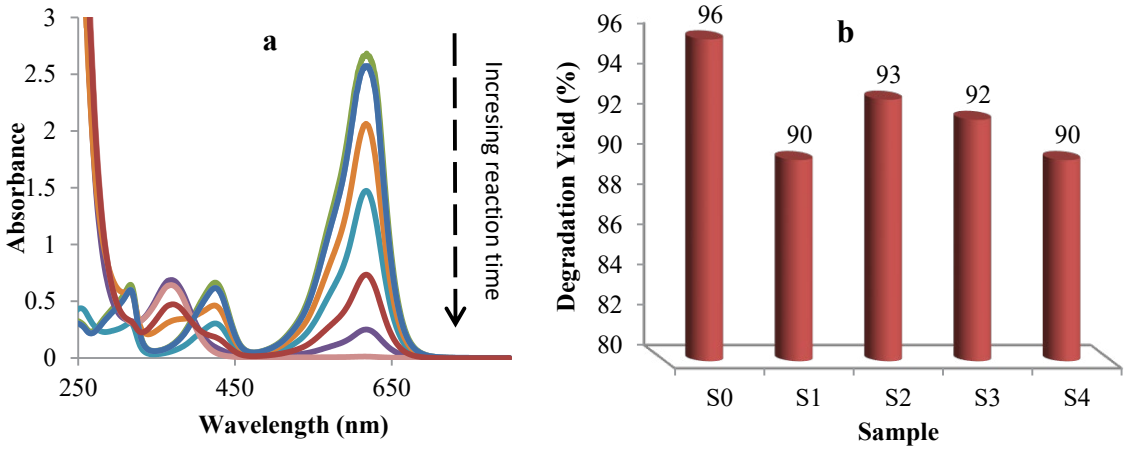

Fig. 8. a) MG degradation spectra by S_0, b) degradation yields of MG by the as-synthesized nanomaterials.

Effect of different parameters on the photocatalytic degradation

The optimal conditions were obtained by design expert software for S_0. It was found that the optimum condition was 0.04 mL H_2O_2, 30 mg catalyst, and 35 min reaction time. The volume and concentration of the as prepared MG solution were 70 mL and 45 ppm, respectively, for obtaining the optimum conditions.

Fig. 9 shows the dye degradation graphs for the obtained materials at the optimum conditions. Fig. 9a, shows the effect of dye concentration on the degradation yield. It is clear that the dye degradation percent is high when the dye concentration is in the range of 45 to 60 ppm. However, when the dye concentration is increased more up to 75 ppm, the degradation yield is decreased. It seems that when the dye concentration is high, light wavelength cannot be penetrated into the dye solution (light screening effect) and the availability of active catalyst sites for MG molecules for adsorption and reaction is reduced. Fig. 9 b shows the dye

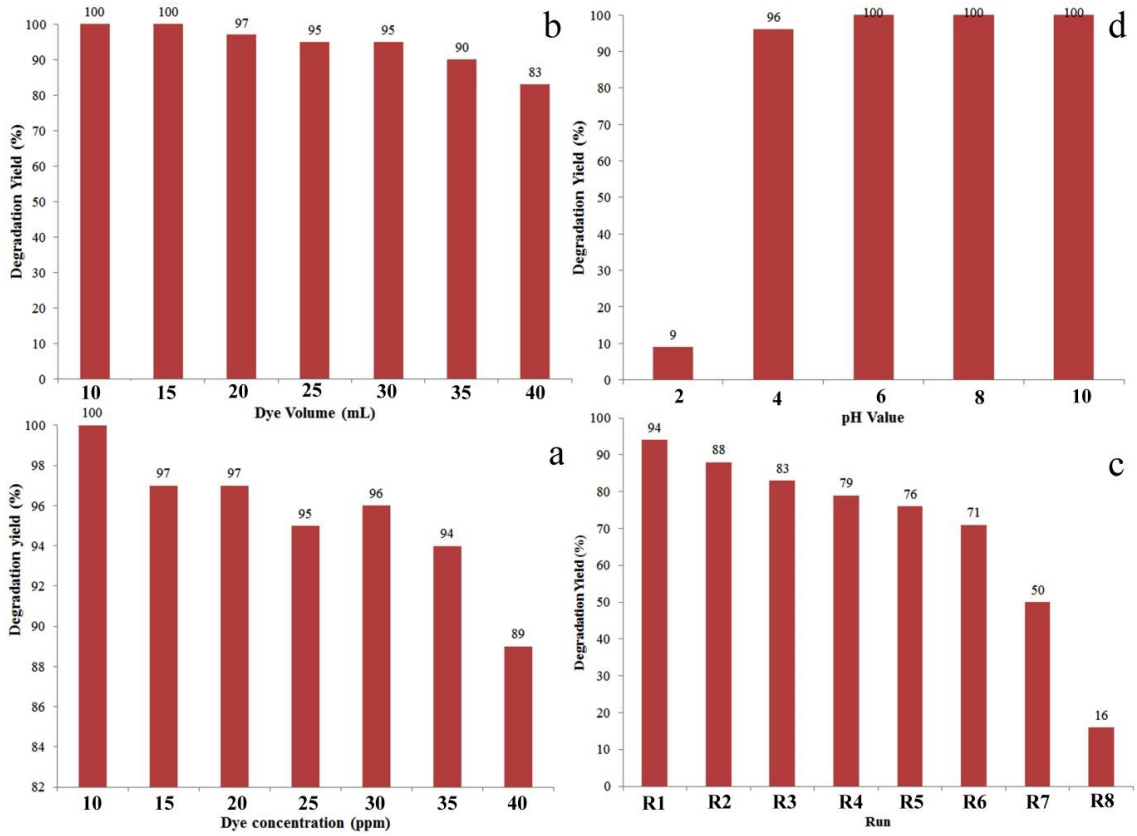

Fig. 9. MG degradation yield (%) at (a) different dye concentrations, (b) different dye volumes, (c) reusability and (d) different dye pH values.

volume effect on the degradation yield. It is found that at the ranges of 70 to 90 mL dye volume, the degradation is high; when the volume is increased up to 100 mL, the degradation is decreased. It can be due to the decreasing the adsorption of dye on the catalyst making the process slower. Fig. 9c shows the reusability of S_0. It indicates that the synthesized catalyst shows considerable reusability performance for the process until run 6. Fig. 9d shows the pH value effect on the degradation yield. It is found that when the pH value is 2, the degradation yield is small. However, when the pH value is increased up to 10, by adding 0.01 M NaOH solution, the degradation yield is increased. The degradation yield is 100% at pH=5 to 10. The parameter pH determines the surface charge properties of the photocatalyst. It can be suggested that the influence of pH on photocatalysis process is due to the amount of dye adsorbed on the photocatalyst. Because MG is a cationic dye, it is conceivable that the adsorption is favored on a negatively charged surface at higher pH values.

Also, we studied the degradation of blank dye solution (without catalyst and H_2O_2) at the optimized condition under the visible light irradiation. It was found that the dye degradation was negligible. Besides, we investigated the degradation process at the optimized condition at the dark room. In the conditions, the degradation yield was nearly zero.

Proposed mechanism for photocatalytic degradation

Converting visible light energy to chemical energy in the photocatalysis reaction by $NiSb_2O_6$ could be similar to previously reported and extensively studied mechanism; in a way that electrons (e^-) and holes (h^+) could be excited under visible light irradiation to the conduction and the valence band edge, respectively. These photo-excited e^- and h^+ then can transfer to the surface of the photocatalyst ($NiSb_2O_6$ particles), where they react with oxidants and reductants,

Table 5. Comparison study of the photocatalytic ability of the $NiSb_2O_6$ with some other catalysts [26].

	Catalyst	Condition	Yield (%)
1	$NiSb_2O_6$ (Present Work)	H_2O_2, 30 mg catalyst, 35 min, visible ligth, 70 mL of 45 ppm MG	97
1	$Sr_2As_2O_7$	H_2O_2, 20 mg catalyst, 33 min, visible ligth, 70 mL of 100 ppm MG	97
2	MoS_2/TiO_2	40 min, sunlight irradiation, 0.1 g catalyst, 10 ppm MG	97
3	$PbCrO_4$	365 ppm MG, 0.1 g catalyst, 4 h, pH=7.5, visible light, 60 min	90
4	TiO_2/ZnO	UV light, pH=7, 50 ppm MG, 1.5 g/L catalyst	100
5	Nix:TiO_2	25 mL of 10 µM MG, UV light	90
6	TiO_2	UV Light, 1 h, 20 mg catalyst, 40 ppm MG	100
7	V doped-ZnO	UV and visible lights, 500 ppm MG, 500 ppm catalyst, 200 min	90
8	$Ni_{1-x}Co_xFe_2O_4$	Sunlight, 50 mL of 25 ppm catalyst, 1 µM MG, H_2O_2, 15 h	100
9	$Pt/TiO_2/SiO_2$	UV and visible lights, 60 min	80
10	Fe^{3+} doped TiO_2	UV and visible lights, 5 ppm MG	85
11	$FeVO_4$	0.03 g catalyst, UV light, 300 min	90
12	TiO_2	UV irradiation, 4 h, 500 ppm catalyst, 50 ppm MG	100
13	Carbon/TiO_2	25 ppm MG, 30 min, pH=8	82-100
14	Mg-doped TiO_2	Vis light, pH=9, 100 ppm MG	89
15	$Ni/MgFe_2O_4$	50 mL of 0.8 g/L MG, 30 mg of catalyst, UV light, pH=4	93
16	La/N co-doped TiO_2 (Ni)	50 W tungsten halogen lamp, 500 mL of 30 ppm MG, 240 min	100
17	UV/H_2O_2	UV lamp (30 W, UV-C), 200 ml MG, 10 ppm, 2 h	100
18	$Cd(OH)_2$-NW-AC	0.06 g catalyst, 50 mL of 15 ppm MG, 35 min	90
19	ZnO-NP-AC	50 mL of 15 ppm MG, 0.015 g catalyst, 35min, pH=7	95
20	Fe_3O_4@Mel	0.3 g catalyst, pH=6.3, 100 mL of 8 ppm MG, 20 min	$9mg_{MG}/g_{cat}$
21	TiO_2/WO_3	pH=12, UV light, 1000 ppm catalyst, 30 min	97
22	$FeSO_4$ -7H_2O	10 mM Fe^{2+}, 40 °C, 25.5 mM H_2O_2, 10 ppm MG	94
23	TiO_2-Co_2O_3	1 ppm MG, using 125 W mercury lamp, 60 min	93
24	SnO_2-CuO	UV light, 20 ppm MG, 0.1 g catalyst, 180 min	96
25	ZnO	4h time, 60 ppm MG, pH=7.5, solar radiation	98
26	Prosopis cineraria	100 mL of 500 ppm MG, 0.4 g PCSD, 3 h	80
27	polyoxometalates	0.1 g catalyst, 200 mL of 0.02 mM of MG, 160 min	65
28	$Zn_xFe_{3-x}O_4$	UV light, 1 g catalyst, 10 µM MG	90
29	S-Me/MA	6 mL of 1000 ppm MG, 50 °C, 24 h, 0.06 g catalyst, pH=10	98
30	Aspergillus flavus	pH=5.8, 150 ppm MG, 8 day	100
31	TiO_2–SiO_2	UV light, H_2O_2, Fe^{2+}, 400 ppm catalyst, 5 ppm MG, 25 min, pH=3	97

respectively, or recombine in the absence of e^- and h^+ traps. The recombination of e^- and h^+ could be greatly minimized in the presence of H_2O_2, which traps the e^- and h^+ to form $^\bullet OH$ and $^\bullet O_2^-$ species [34]. The excited e^- reacts with H_2O_2 to form $HO^\bullet$ and OH^- groups. The formed OH^- group reacts with h^+ and forms $HO^\bullet$ group. Besides, H_2O_2 can trap the photoexcited species in another way. It reacts with h^+ and forms $HO_2^\bullet$ radical and H^+. The produced $HO_2^\bullet$ is decomposed to $^\bullet O_2^-$ and H^+. H_2O as the solvent of the photodegradation reaction can react with h^+ to form $HO^\bullet$ and H^+ species. The produced H^+ ion reacts with the dissolved O_2 and $2e^-$ and forms the initial H_2O_2. The dissolved O_2 can also react with e^- to form $^\bullet O_2^-$. The so-formed $^\bullet OH$ or $^\bullet O_2^-$ species are used for the decomposition of organic contamination molecules such as MG to intermediates or mineralized products through oxidation reactions [35-37].

$$NiSb_2O_6 + h\nu \rightarrow h^+ (NiSb_2O_6) + e^- (NiSb_2O_6) \quad (1)$$

$$H_2O_2 + e^- (NiSb_2O_6) \rightarrow HO^\bullet + OH^- \quad (2)$$

$$OH^- + h^+ (NiSb_2O_6) \rightarrow HO^\bullet \quad (3)$$

$$H_2O_2 + h^+ (NiSb_2O_6) \rightarrow HO_2^\bullet + H^+ \quad (4)$$

$$HO_2^\bullet \rightarrow \bullet O_2^- + H^+ \quad (5)$$

$$H_2O + h^+ (NiSb_2O_6) \rightarrow HO^\bullet + H^+ \quad (6)$$

$$2H^+ + O_2 + 2e^- \rightarrow H_2O_2 \quad (7)$$

$$O_2 + e^- (NiSb_2O_6) \rightarrow \bullet O_2^- \quad (8)$$

$$MG + OH^\bullet + \bullet O_2^- \rightarrow \text{degradation product} \quad (9)$$

At high amounts of H_2O_2 volume, the photodegradation yield maybe decreased. It is because the produced highly reactive hydroxyl radical (eq. 11) may react with excess amount of H_2O_2 and produces hydroperoxyl radical ($HO_2^\bullet$) (eq.12) which is less reactive and ultimately

inhibits the degradation with producing O_2 and H_2O in (eq.14). The reaction mechanism is explained below [38, 39]:

$$H_2O_2 + e^- \left(NiSb_2O_6\right) \rightarrow HO^{\bullet} + OH^- \quad (10)$$

$$OH^- + h^+ \left(NiSb_2O_6\right) \rightarrow HO^{\bullet} \quad (11)$$

$$H_2O_2 + HO^{\bullet} \rightarrow HO_2^{\bullet} + H_2O \quad 12 \quad (12)$$

$$H_2O_2 + HO_2^{\bullet} \rightarrow HO^{\bullet} + O_2 + H_2O \quad 13 \quad (13)$$

$$HO^{\bullet} + HO_2^{\bullet} \rightarrow O_2 + H_2O \quad (14)$$

To show the merit of the present work, we have compared $NiSb_2O_6$ nanocatalyst results with some of the previously reported catalysts for the degradation of MG (Table 5). It is clear that $NiSb_2O_6$ showed greater activity than some other heterogeneous catalysts. Besides, the data reveal that the high yield of the photodegradation was achieved by the application of visible light condition in this work.

CONCLUSION

The novelty of the present work was doping new dopant ions into $NiSb_2O_6$ crystal system by a novel method, introducing a new application of the material as a high performance nano-photocatalyst to remove water pollutant dye under visible light irradiation, and presenting several analyses to study the physical properties of the obtained materials. The present work studied the synthesis of highly crystalline $NiSb_2O_6$ nanomaterials via one-step facile solid state method. Some lanthanide ions such as Eu, Gd, Ho and Yb were doped into $NiSb_2O_6$ crystal system. The XRD patterns indicated that $NiSb_2O_6$ was crystallized well in orthorhombic crystal system under the present solid state condition. The morphology of the obtained materials was sponge. FESEM images revealed that the particle sizes of the doped materials were smaller than those of pure $NiSb_2O_6$. The photocatalytic data indicated that the obtained materials had excellent efficiency for the removal of MG from aqueous solution. It was found that the optimum condition was 0.04 mL H_2O_2, 30 mg catalyst and 35 min reaction time. It was found that the catalytic performance was excellent when the pH value was in the range of 4 to 10, the dye concentration was up to 60 ppm and the dye volume was up to 90 mL.

CONFLICTS OF INTEREST

The authors do not have any personal or financial conflicts of interest.

REFERENCE

[1] Nikulin A. Y., Zvereva E. A., Nalbandyan V. B., Shukaev I. L., Kurbakov A. I., Kuchugura M. D., Raganyan G. V., Popov Y. V., Ivanchenko V. D., Vasiliev A. N., (2017), Preparation and characterization of metastable trigonal layered MSb_2O_6 phases (M = Co, Ni, Cu, Zn, and Mg) and considerations on $FeSb_2O_6$. *Dalton Trans*. 46: 6059-6068.

[2] Shengsong G., Qingyao W., Qian S., Yuhua Z., Xiaokun Y., Xiaojie W., (2011), Hydrothermal synthesis of morphology-controllable Sb_2O_3 microstructures: Hollow spindle-like and cobblestone-like microstructures. *s* 257: 3657–3665.

[3] Jiao S., Pang G., Liang H., Chen Y., Feng S., (2007), Hydrothermal synthesis and magnetic properties of $CuSb_2O_6$ nanoparticles and nanorods. *J. Nanopart. Res*. 9: 605-610.

[4] Singh A., Singh A., Singh S., Tandon P., (2016), Nickel antimony oxide ($NiSb_2O_6$): A fascinating nanostructured material for gas sensing application. *Chem. Phys. Lett*. 646: 41-46.

[5] Westin G., Nygren M., (1993), Sol-Gel Preparation of M-Sb oxides from Sb (OBu"), -M-Acetate precursors with M = Mn, Co, Ni. *J. Mater. Chem*. 3: 367-371.

[6] Singh J., Bhardwaj N., Uma S., (2013), Single step hydrothermal based synthesis of M(II)Sb_2O_6 (M = Cd and Zn) type antimonates and their photocatalytic properties. *Bull. Mater. Sci.* 36: 287-291.

[7] Larcher D., Prakash A. S., Laffont L., Womes M., Jumas J. C., Olivier-Fourcade J., Hedge M. S., Tarascon J. M., (2006), Reactivity of antimony oxides and MSb_2O_6, M = Cu, Ni, Co…, trirutile-type phases with metallic Lithium. *J. Electrochem. Soc*. 153: 1778-1787.

[8] Ehrenberg H., Wltschek G., Rodriguerz-Carvajal J., Vogt T., (1998), Magnetic structure of the tri-rutiles $NaTa_2O_6$ and $NiSb_2O_6$. *J. Magn. Magn. Mater*. 184: 111-115.

[9] Bonilla H. G., Betancourtt V. M. R., Bonilla J. T. G., Mortinz M. F., Bonilla A. G., Gonzalez M. A., Salazar S. S. S., Ortiz L. G., (2016), Synthesis and characterization of Nanostructured $NiSb_2O_6$ powders. IX International conference in surfaces'', materials and vacuum. September 26 th – 30 th, Mexico. Page 259.

[10] Hakimyfard A., (2017), Effects of reaction temperature and raw material type on optical properties and crystal phase growth of Solid state synthesized $NiSb_2O_6$ nanomaterials. *J. Adv. Mater. Proc*. 5: 56-65.

[11] Srivastava S., Sinha R., Roy D., (2004), Toxicological effects of malachite green. *Aquatic toxicology*. 66: 319-329.

[12] Tolia J., Chakraborty M., Murthy Z., (2012), Photocatalytic degradation of malachite green dye using doped and undoped ZnS nanoparticles. *Pol. J. Chem. Technol*. 14: 16-21.

[13] Chen C., Lu C., Chung Y., Jan J., (2007), UV light induced photodegradation of malachite green on TiO_2 nanoparticles. *J. Hazard. Mater*. 141: 520-528.

[14] Kusuma H. S., Sholihuddin R. I., Harsini M., Darmokoesoemo H., (2016), Electrochemical degradation of malachite green dye using Carbon/TiO_2 electrodes. *J. Mater. Environ. Sci*. 7: 1454-1460.

[15] Miranzadeh M., Afshari F., Khataei B., Kassaee M., (2020),

Adsorption and photocatalytic removal of arsenic from water by a porous and magnetic nanocomposite: Ag/TiO_2/Fe_3O_4@GO. *Adv. J. Chem. A*. 3: 408-421.

[16] Sajjadnejad M., Karimi Abadeh H., (2020), Processing of nanostructured TiO_2 and modification of its photocatalytic behavior for methylene blue degradation. *Adv. J. Chem. A*. 3: 422-431.

[17] Hu K.-h., Meng M., (2013), Degradation of malachite green on MoS_2/TiO_2 nanocomposite. *Asian J. Chem.* 25: 5827-5829.

[18] Ameta K., Tak P., Soni D., Ameta S. C., (2014), Photocatalytic decomposition of malachite green over lead chromate powder. *Sci. Rev. Chem. Commun*. 4: 38-45.

[19] Bansal P., Bhullar N., Sud D., (2009), Studies on photodegradation of malachite green using TiO_2/ZnO photocatalyst. *Desalin. Water Treat*. 12: 108-113.

[20] Soni H., JI N. K., (2014), UV light induced photocatalytic degradation of malachite GREEN on TiO_2 nanoparticles. *Int. J. Recent Res. Rev*. 7: 10-15.

[21] Sols-Casados D., Escobar-Alarcn L., Fernndez M., Valencia F., (2013), Malachite green degradation in simulated wastewater using Ni_x : TiO_2 thin films. *Fuel*. 110: 17-22.

[22] Khezami L., Taha K. K., Ghiloufi I., El Mir L., (2016), Adsorption and photocatalytic degradation of malachite green by vanadium doped zinc oxide nanoparticles. *Water Sci. Technol*. 73: 881-889.

[23] Jo W.-K., Parka G. T., Tayade R. J., (2014), Synergetic effect of adsorption on degradation of malachite green dye under blue LED irradiation using spiral-shaped photocatalytic reactor. *J. Chem. Technol. Biotechnol*. 90: 2280-2289.

[24] He H-Y., (2015), Photocatalytic degradations of malachite green on magnetically separable $Ni_{1-x}Co_xFe_2O_4$ nanoparticles synthesized by using a hydrothermal process. *Amer. Chem. Sci. J.* 6: 58-68.

[25] Afshar S., Samari Jahromi H., Jafari N., Ahmadi Z., Hakamizadeh M., (2011), Degradation of malachite green oxalate by UV and visible lights irradiation using Pt/TiO_2/SiO_2 nanophotocatalyst. *Sci. Iran*. 18: 772-779.

[26] Khademinia S., Behzad M., Kafi-Ahmadi L., Hadilou S., (2018), Hydrothermally synthesized strontium arsenate nanomaterial through response surface methodology. *Z. Anorg. Allg. Chem*. 644: 221-227.

[27] Hosseiny Davarani S. S., Rezayati zad Z., Taheri A. R., Rahmatian N., (2017), Highly selective solid phase extraction and preconcentration of Azathioprine with nano-sized imprinted polymer based on multivariate optimization and its trace determination in biological and pharmaceutical samples. *Mater. Sci. Eng. C.* 71: 572–583.

[28] Abdollahi F., Taheri A., Shahmari M., (2019), Application of selective solid-phase extraction using a new core-shell-shell magnetic ionimprinted polymer for the analysis of ultra-trace mercury in serum of gallstone patients. *Sep. Sci. Technol.* https://doi.org/10.1080/01496395.2019.1651337.

[29] Lee J. W., Lee J. K., Cho S. K., Jung J. S., Lee S. H., (2004), Partial oxidation of methane over M-Sb-Te-O (M = Transition Metal) catalysts. *Bull. Korean Chem. Soc*. 25: 573-576.

[30] Alabdeen S. Z., Ismail I., (2016), Studying the structural changes of $NiSb_2O_4$ by temperature using Sol-Gel method. *Chem. Mater. Res*. 8: 13-17.

[31] Naidu B. S., Pandey M., Sudarsan V., Tewari R., Vats R. K., (2011), Interaction of Sb^{3+} ions with Eu^{3+} ions during the room temperature synthesis of luminescent Sb_2O_3 nanorods: Probed through Eu^{3+} luminescence. *Appl. Sur. Sci.* 257: 3657–3665.

[32] Kim S. S., Na H. G., Kwon Y. J., (2015), Synthesis and room-temperature NO_2 sensing properties of Sb_2O_5 nanowires. *Met. Mater. Int.* 21**:** 415–421.

[33] Leineweber A., Jacobs H., Hull S., (2001), Ordering of nitrogen in nickel nitride Ni_3N determined by neutron diffraction. *Inorg. Chem*. 40: 5818-5822.

[34] Hosseinpour Z., Alemi A., Khandar A. A., Zhao X., Xie Y., (2015), A controlled solvothermal synthesis of CuS hierarchical structures and their natural-lightinduced photocatalytic properties. *New J. Chem*. 39: 5470-5746.

[35] Magdalane C. M., Kaviyarasu K., Vijaya J. J., Siddhardha B., Jeyaraj B., (2016), Photocatalytic activity of binarymetal oxide nanocomposites of CeO_2/CdO nanospheres: Investigation of optical and antimicrobial activity. *J. Photochem. Photobiol. B: Biol*. 163: 77-86.

[36] Tolia J. V., Chakraborty M., Murthy Z. V. P., (2012), Photocatalytic degradation of malachite green dye using doped and undoped ZnS nanoparticles. *Pol. J. chem. Technol*. 14: 16-21.

[37] Deepa N., Meghna P., Kandasamy S., (2014), Experimental studies on decolonisation of malachite dye using continuous photocatalytic reactor. *Int. Res. J. Environ. Sci*. 3: 14-21.

[38] Hameed B. H., Lee T. W., (2009), Degradation of malachite green in aqueous solution by Fenton process. *J. Hazard. Mater*. 164: 468-472.

[39] Abilarasu A., Somanathan T., Saravanan A., Saravanan V., Rajakumar P., (2016), Enhanced photocatalytic degradation of malachite green on spinel ferrite (Nickel/Magnesium Ferrite) under direct sun light. *Sci. Bio. Pharma. J. Int*. 7: 93-99.